CrystEngComm

ROYAL SOCIETY OF CHEMISTRY

PAPER

View Article Online
View Journal | View Issue

Cite this: *CrystEngComm*, 2025, **27**, 4835

Interface engineering of RuO_2/Ru–Co_3O_4 heterostructures for high-efficiency oxygen evolution in acid†

Yixuan Yuan, [ab] Chang Liu, [ab] Shanshan Liu, [a] Ruimin Ding *[a] and Xi Yin *[a]

Proton exchange membrane water electrolysis (PEMWE) powered by renewable electricity is a promising technology for green hydrogen production. Ru-based catalysts are a cost-effective alternative to Ir-based counterparts for the oxygen evolution reaction (OER), yet achieving balanced activity and stability remains challenging. In this study, we optimize the performance of RuO_2 by constructing RuO_2/Ru–Co_3O_4 heterogeneous interfaces. Our results indicate that RuO_2/Ru–Co_3O_4 catalyst pyrolyzed at lower temperatures exhibits uniformly small particle sizes with abundant heterointerfaces and strong interfacial electronic interactions. Elevated pyrolysis temperatures enlarge catalyst particle sizes, simultaneously decreasing heterointerfaces and weakening the interfacial interactions. In rotating disk electrode experiments, the mass activity of the RuO_2/Ru–Co_3O_4 catalysts is significantly improved compared to the commercial RuO_2. This improvement is attributed to the heterogeneous interfaces, which offer greater utilization of active sites and enhanced charge transfer capabilities. Furthermore, the mass activity of the RuO_2/Ru–Co_3O_4 catalysts decreases with increasing pyrolysis temperatures due to the reduction in heterogeneous interfaces. Additionally, the stability of the RuO_2/Ru–Co_3O_4 catalysts is notably superior to that of commercial RuO_2, owing to the interfacial electronic interactions. However, this stability is negatively impacted by higher pyrolysis temperatures as the interfacial electronic interactions weaken. In preliminary membrane electrode assembly tests, the RuO_2/Ru–Co_3O_4 catalyst with low Ru loading shows higher activity than commercial RuO_2. Further triple-phase boundary optimization of the catalyst layer is needed. These findings contribute to advanced RuO_2-based catalyst design for PEMWE.

Received 7th May 2025,
Accepted 28th May 2025

DOI: 10.1039/d5ce00474h

rsc.li/crystengcomm

Introduction

Renewable electricity-powered proton exchange membrane water electrolysis (PEMWE) technology has garnered considerable acclaim for its superior energy efficiency, high current density, and exceptional hydrogen purity in green hydrogen production.[1–4] This technology hinges on Ir-based catalysts to facilitate the oxygen evolution reaction (OER) under challenging acidic and oxidative conditions.[5–8] However, the high cost and scarce availability of Ir significantly hinder its widespread application. In contrast, Ru-based catalysts, notably RuO_2, offer a compelling alternative.[9–11] These catalysts are approximately one-tenth the price of Ir-based catalysts and demonstrate high intrinsic activity. Further improving the OER performance of RuO_2 is crucial for advancing its application in PEMWE.[12–14]

Two principal mechanisms govern the acidic OER catalyzed by RuO_2: the adsorbate evolution mechanism (AEM) and the lattice oxygen oxidation mechanism (LOM).[15–17] In the AEM, the RuO_2 catalyst demonstrates commendable stability, but the scaling relationship between the adsorption energies of intermediates constrained its activity. In contrast, its activity in the LOM improves, but its stability decreases due to structural collapse.[18,19] Various strategies have been developed to address the trade-off between catalytic activity and structural stability. These strategies include the hybridization of RuO_2 with Ir,[20,52] the introduction of stable supports to anchor RuO_2,[21,53] chemical doping with other elements to regulate the valence state of Ru,[22,54] and the formation of a solid solution.[23,55] These strategies have proven effective in improving both the catalytic performance and structural stability of RuO_2, providing valuable insights for designing advanced OER catalysts.[20–23]

Among various strategies, one of the most extensively studied is the introduction of supports, such as TiO_2, CeO_2, WO_3, MnO_2, and MoO_3, to anchor Ru ions.[24–28] These

[a] *State Key Laboratory of Coal Conversion, Institute of Coal Chemistry, Chinese Academy of Sciences, Taiyuan, Shanxi 030001, China. E-mail: dingrm@sxicc.ac.cn, xiyin@sxicc.ac.cn*
[b] *School of Chemical Engineering, University of Chinese Academy of Sciences, Beijing 100049, China*

† Electronic supplementary information (ESI) available. See DOI: https://doi.org/10.1039/d5ce00474h

supports could create synergistic interactions with the active sites, boosting activity and extending their operational lifetime. One recent work developed a RuO_2/MnO_2 heterostructure with MnO_2 acting as an electron reservoir for RuO_2. In this nanostructure, MnO_2 facilitates electron transfer from RuO_2, enhancing the OER activity, and donates electrons to RuO_2, improving its stability.[27] Another study designed RuO_2/MoO_3 catalysts with abundant and intimate interfaces to enable the reactive *O intermediate spillover from RuO_2 to MoO_3. The RuO_2/MoO_3 catalysts demonstrate both high activity and stability owing to the oxygen spillover process that helps suppress over-oxidation and dissolution of RuO_2.[28]

Spinel Co_3O_4, whose theoretical activity is comparable to RuO_2, has also been explored as support for RuO_2. Extensive studies have shown that the stability and activity of RuO_2/Co_3O_4 composites are significantly improved due to electron transfer between Ru and Co.[29–32] These findings provide valuable insights for further developing RuO_2/Co_3O_4 catalysts. By optimizing interfacial interactions and structural design, it is possible to achieve more significant performance gains, addressing the key challenge of balancing activity and stability of RuO_2.

Building on this foundation, we synthesized a series of RuO_2/Ru–Co_3O_4 (RCO) catalysts by pyrolyzing Ru/ZIF-67 at controlled temperatures. Small particle sizes, abundant interfacial contacts, and strong interactions between RuO_2 and Co_3O_4 characterize the RCO catalysts. As the pyrolysis temperature increases, the particle size of the catalysts grows while the interfacial interaction between RuO_2 and Co_3O_4 weakens. In the rotating disk electrode (RDE) experiments, the RCO catalysts demonstrate significantly enhanced mass activity (MA) and stability compared to commercial RuO_2. Among these, the RCO catalyst synthesized at low temperatures exhibits the most significant increase in MA due to its abundant heterointerfaces, which provide the largest electrochemical active surface area (ECSA) and lowest charge transfer resistance (R_{ct}). Additionally, this low-temperature synthesized RCO catalyst demonstrates the greatest improvement in stability, attributed to its strong interfacial electronic interactions. During membrane electrode assembly (MEA) testing, the RCO catalyst, which features low Ru loading, shows superior activity to commercial RuO_2. However, the porous structure of the catalyst layer hinders the establishment of a triple-phase boundary. These findings highlight the promising potential of RCO catalysts for efficient green hydrogen production while emphasizing the need for further optimization to overcome structural constraints in PEMWE applications.

Experimental

Materials

Cobalt(II) nitrate ($Co(NO_3)_2{\cdot}6H_2OO$, 99.7%, hexahydrate, Macklin, China), 2-methylimidazole (2-MIM, $C_4H_6N_2$, ≥98%, Aladdin, China), ruthenium trichloride hydrate ($RuCl_3{\cdot}xH_2O$, Tianjin Baima Technology Co. LTD, China), ruthenium(IV) oxide (RuO_2, ≥99.9%, Aladdin, China), Pt/C (70 wt% Pt, HiCaP 70, CASI NEW Energy Technology (Ningbo) Co., Ltd, China), perchloric acid ($HClO_4$, for analysis, *ca.* 70% solution in water, Thermo Scientific Chemicals, America), isopropanol (IPA, >99.7%, analytical reagent grade, Kermel, China), methanol anhydrous (MeOH, ≥99.5%, analytical reagent grade, SCR, China), deionized water (DI water, Milli-Q, 18.2 MΩ cm at 25 °C), ultrapure nitrogen (N_2, 99.999%), ultrapure oxygen (O_2, 99.999%), and a Nafion D521 dispersion (5 wt%, EW = 1100, Alfa Aesar) were used as received.

Synthesis of the ZIF-67

To prepare ZIF-67, 2.91 g (10 mmol) of $Co(NO_3)_2{\cdot}6H_2O$ and 3.284 g (40 mmol) of 2-MIM were separately dissolved in 20 ml of methanol to form clear solutions. The 2-MIM solution was then quickly added to the $Co(NO_3)_2{\cdot}6H_2O$ solution and sonicated for 30 minutes in an ultrasonic bath. This mixture was stirred at 600 rpm for 18 h at room temperature. Finally, the precipitate was collected, rinsed 3 times with methanol, and dried under vacuum at 60 °C for about 1 h to obtain ZIF-67.

Synthesis of the Ru/ZIF-67

First, 0.33 g of ZIF-67 and 0.08 g of $RuCl_3{\cdot}xH_2O$ were separately added to 15 mL of DI water and sonicated for 5 min. The dispersion of ZIF-67 was then quickly added to the $RuCl_3{\cdot}xH_2O$ solution in an ultrasonic bath and sonicated continuously for another 45 minutes. Finally, the mixture was filtered and dried to obtain the precursor, Ru/ZIF-67, with Ru ions loaded on ZIF-67.

Synthesis of the RuO_2/Ru–Co_3O_4 catalysts

The obtained Ru/ZIF-67 was annealed separately at 300, 350, 400, and 450 °C for 3 h in air at a heating rate of 2 °C min^{-1}. The resulting samples are denoted as RuO_2/Ru-Co_3O_4_*T* and abbreviated as RCO_*T*, where *T* represents the annealing temperature. In addition, ZIF-67 was heat-treated at 350 °C to prepare a control sample of Co_3O_4.

Physical characterizations

A high-resolution transmission electron microscope (HR-TEM, JEM-2100F, JEOL, Japan) equipped with an energy dispersive spectrometer (EDS), a scanning electron microscope (SEM, JSM-7001F, JOEL, Japan), a thermal gravimetric (TG) and derivative thermogravimetric (DTG) analysis (TMA7100, Hitachi, Japan), a powder X-ray diffraction diffractometer (XRD, Bruker D8-Advance-A25, Britain), an X-ray photoelectron spectroscopy (XPS, Thermo Scientific, America), and inductively coupled plasma mass spectrometry (ICP-MS, NexION 5000, PerkinElmer Inc, America) were used to characterize the obtained samples. The Ru, Co, and Pt loadings in PEMWE were measured using

an X-ray fluorescence spectrometer (XRF, ARL QUANT'X EDXRF Analyzer, Thermo Fisher Scientific Inc, America).

Electrochemical measurements

Electrochemical measurements were conducted using a three-electrode system controlled by a Pine Research MSR rotator (Pine Research Instrumentation Co. Ltd, America) and a bipotentiostat (CHI 760E, CH Instruments, Inc., China). The experiment utilized a five-necked electrochemical cell containing 0.10 M $HClO_4$ solution. A rotating disk electrode (RDE, Pine Research Instrumentation Co. Ltd, America) with a glassy carbon electrode (GCE, 5 mm diameter) was used as the working electrode. A graphite rod served as the counter electrode, and an Ag/AgCl (KCl, saturation) electrode was employed as the reference electrode. The Ag/AgCl electrode was calibrated to a reversible hydrogen electrode (RHE), which was constructed by continuously bubbling pure H_2 gas onto a Pt coil electrode placed in a glass tube filled with the electrolyte solution.

The catalyst ink was prepared by dispersing 2 mg of catalyst in a mixture of DI-water (200 μL), IPA (200 μL), and D521 Nafion dispersion (4 μL, 5 wt%) in a sonication bath for 1 hour. Then, electrodes with a catalyst loading of 0.500 mg cm^{-2} for RCO_*T* were prepared by depositing 19.8 μL of the ink onto the GCE. For comparison, 7.28 μL of commercial RuO_2 ink and 12.44 μL of Co_3O_4 ink were deposited on GCE to obtain loadings of 0.186 mg cm^{-2} and 0.314 mg cm^{-2}, respectively. The Ru mass (m_{Ru}) loadings for RCO_*T* and commercial RuO_2 were calculated to be 0.141 mg cm^{-2}. The Co mass (m_{Co}) loadings for RCO_*T* and Co_3O_4 were calculated to be 0.230 mg cm^{-2}.

Cyclic voltammograms (CVs) were recorded at varying scan rates (v) from 40 to 120 mV s^{-1} in an N_2-saturated 0.10 M $HClO_4$ solution, with the potential window set at ± 50 mV *vs.* the open-circuit potential (OCP). Linear sweep voltammograms (LSVs) were recorded from 1.1 to 1.55 V *vs.* RHE at a scan rate of 5 mV s^{-1} in an O_2-saturated 0.10 M $HClO_4$ solution, with a rotation rate set at 1600 rpm. Unless noted, all the LSV tests were corrected with 100% internal resistance (iR) compensation. The durability was assessed through chronopotentiometry testing at a constant current density of 10 mA cm^{-2}. Electrochemical impedance spectroscopy (EIS) measurements were performed at 1.5 V *vs.* RHE within a 100 kHz–0.1 Hz frequency range.

The electrochemically active surface areas (ECSAs) for RCO_*T*, commercial RuO_2, and Co_3O_4 were estimated from the electrochemical double-layer capacitance (C_{dl}) of the catalytic surfaces. The C_{dl} is determined from the slope of the plot of i_C *vs.* v in CV, where i_C is the charging current at the OCP corresponding to v. ECSA was calculated using the equation:

$$\mathrm{ECSA} = \frac{C_{dl}}{C_s} A \tag{1}$$

where A is the area of GCE, C_s is the specific capacitance of an atomically smooth planar surface of the material per unit area under identical electrolyte conditions. A value of 0.040 mF cm^{-2} was used for C_S, which is based on the typical reported values.[51]

The Tafel plots were derived from the following equation:

$$\eta = a + b \log j \tag{2}$$

where η is the overpotential, defined as the difference between the potential of an electrode and its equilibrium potential (E_{eq}, E_{eq} = 1.23 V *vs.* RHE), j is the current density, a is the intercept at the y-axis, and b is the Tafel slope.

The mass activity (MA) was calculated using the equation:

$$\mathrm{MA} = \frac{j}{m_{Ru}} \tag{3}$$

The specific activity (SA) was calculated using the equation:

$$\mathrm{SA} = \frac{i}{\mathrm{ECSA}} \tag{4}$$

PMEWE tests

Anode catalyst inks were prepared by mixing RCO_350 or commercial RuO_2 catalysts with Nafion D521 ionomer dispersion in a mixture of DI-water and IPA, followed by ultrasonication for 30 min. The catalyst concentration was 6.1 mg mL^{-1}. The volume ratio of DI-water to IPA was 0.042. The weight ratio of the ionomer to catalyst was 0.42.

A commercial Pt/C catalyst was used as the cathode catalyst. The cathode catalyst ink was prepared using a method similar to that of the anode. The catalyst concentration was 2.1 mg mL^{-1}. The weight ratio of the ionomer to carbon was 0.6.

The catalyst-coated membrane (CCM) with an active area of 5 cm^2 was prepared by ultrasonically spraying the anode inks onto one side of the Nafion® NR115 membranes at 60 °C, followed by spraying the cathode inks on the other side. The anode loadings were *ca.* 0.26 mg_{Ru} cm^{-2} for RCO_350 and *ca.* 0.90 mg_{Ru} cm^{-2} for commercial RuO_2. The cathode loading was *ca.* 0.40 mg_{Pt} cm^{-2}. These loadings were measured using an XRF. The obtained CCM was assembled with two porous transport layers, two polytetrafluoroethylene gaskets, a titanium felt with a 5 cm^2 flow field, a graphite bipolar plate also featuring a 5 cm^2 flow field, and two metal current collectors to complete the full PMEWE.

During the PEMWE operation, DI water was pumped into the anode and circulated between the anode and a glass flask at a 100 mL min^{-1} flow rate. A bias voltage was applied using a high-current electrochemical workstation (VersaSTAT 3F, Princeton Applied Research, AMETEK Inc, America). The current–voltage (I–V) curves were recorded by polarizing the anode from 1.2 to 1.8 V *vs.* RHE at a scan rate of 10 mV s^{-1}.

Results and discussion

The morphology and composition of RCO_*T* catalysts

Scheme 1 illustrates the synthesis strategy for RCO_*T* catalysts. ZIF-67 was synthesized as a precursor for the Co_3O_4 support. The pore size of ZIF-67 is 0.34 nm, which allows the

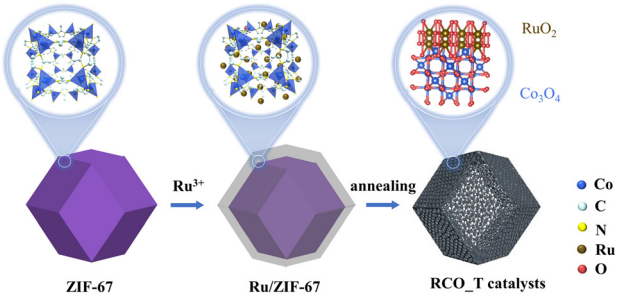

Scheme 1 Schematic illustration for the synthesis of RCO_*T* catalysts.

impregnated Ru^{3+} to pass through the pore channel and adsorb around CoN_4 units.[33] Subsequently, during the *in situ* conversion process under heating, oxygen diffuses into the micropore, forming RCO_*T* catalysts with contact-rich interfaces. We first examined the impregnation of Ru^{3+} within ZIF-67. Fig. S1 and S2† show that ZIF-67 and Ru/ZIF-67 possess dodecahedral structures. However, the surfaces of Ru/ZIF-67 appear rougher compared to ZIF-67. EDS elemental mappings (Fig. S3†) show distinct Ru, Co, and N signals, revealing a uniform Ru dispersion within the ZIF-67 framework. XRD patterns for both ZIF-67 and Ru/ZIF-67 (Fig. S4†) suggest no noticeable difference, indicating that the introduction of Ru^{3+} does not alter the crystal structure of ZIF-67.[34] Consequently, we speculated that the Ru^{3+} is effectively adsorbed within the ZIF-67. It is further supported by ICP-MS analysis, which confirms a Co : Ru atomic ratio of *ca.* 2.8 : 1 (Table S1†).

We then elucidated the formation process of RCO_*T* catalysts under different annealing temperatures. The TG-DTG curves (Fig. S5†) indicate that ZIF-67 decomposition begins at 330.3 °C (mass loss onset), with a sharp mass loss of 52.97% peaking at 375.0 °C. This peak corresponds to the collapse of the ZIF-67 framework and the formation of Co_3O_4.[35] Literature reports also confirm that $RuCl_3$ converts to RuO_2 above 300 °C.[36] To prevent the agglomeration of the catalyst caused by high temperature, we finally chose a pyrolysis temperature range of 300–450 °C. Fig. 1a shows the XRD patterns of RCO_*T* catalysts synthesized at different temperatures. At 300 °C, two broad peaks are evident at 31.3 and 36.9°, corresponding to the (220) and (311) plane of Co_3O_4 (PDF #73-1701), without signals from RuO_2. We hypothesize that Ru remains in a non-oxidized state or is amorphous at this temperature. Upon increasing the temperature to 350 °C, distinct diffraction peaks associated with RuO_2 (PDF #73-1469) emerge, indicating the formation of RuO_2. Concurrently, the diffraction peaks of Co_3O_4 become

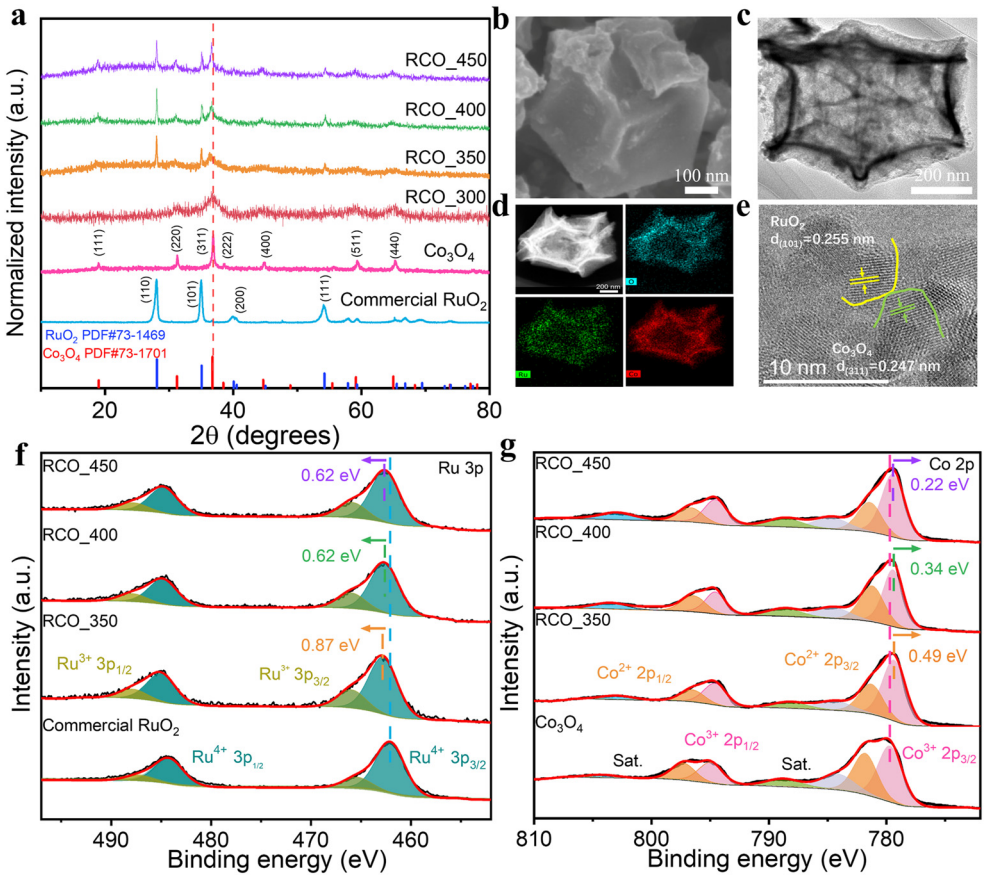

Fig. 1 Phase and structural characterization: (a) XRD patterns of Co_3O_4, RuO_2, and RCO_*T* catalysts. (b–e) SEM image, TEM image, EDS elemental mappings, and HR-TEM image of typical RCO_350. (f) Deconvoluted high-resolution Ru 3p XPS spectra of the commercial RuO_2 and RCO_*T* catalysts. (g) Deconvoluted high-resolution Co 2p XPS spectra of the Co_3O_4 and RCO_*T* catalysts.

more pronounced. These diffraction peaks shift slightly towards lower angles, likely attributed to incorporating larger Ru atoms into the Co_3O_4 lattice.[37] As the calcination temperature is raised to 400 and 450 °C, the crystallinity of the RCO_*T* catalysts is further improved, as evidenced by the enhanced peak intensities. The central diffraction peaks of Co_3O_4 remain consistent with those observed at 350 °C, suggesting that temperature variations within this range do not significantly influence the doping of Ru. These results indicate that RuO_2 and Ru-doped Co_3O_4 generation begins at 350 °C, with their crystallinity enhancing as the annealing temperature increases.

SEM and TEM analyses (Fig. S6 and S7† and 1b and c) reveal that the RCO_*T* catalysts exhibit porous dodecahedral architectures. The EDS mappings of typical RCO_350 in Fig. 1d demonstrate a homogenous distribution of Ru, O, and Co elements, suggesting significant interfacial contact between RuO_2 and Ru–Co_3O_4. Furthermore, the HR-TEM analysis of typical RCO_350 in Fig. 1e confirms the presence of heterointerfaces. Ultrasmall RuO_2 nanoparticles, *ca.* 5 nm in size, are observed on the surface of similarly sized Co_3O_4 nanoparticles, characterized by crystal planes (101) and (111) with *d*-spacing of 0.255 and 0.247 nm, respectively. Additionally, in Fig. S8,† the particle size slightly increases, and the boundaries between particles become more distinct as the calcination temperature increases from 350 to 450 °C. These findings suggest that the heating conversion process forms RCO_*T* catalysts with small particle sizes and contact-rich interfaces.

The elemental compositions and valence states of RCO_*T* catalysts, Co_3O_4, and commercial RuO_2 were examined using XPS. The XPS spectra of the RCO_*T* catalysts confirm the presence of Co, Ru, O, and C elements, as shown in Fig. S9.† Furthermore, the O 1s spectra of RCO_*T* catalysts were deconvoluted, revealing three distinct peaks corresponding to lattice O^{2-} (529.35 eV for Co–O and 528.35 eV for Ru–O), O_V (& O–H) (530.75 eV), and O_{ads} (532.5 eV).[38,39] Detailed fitting results were provided in Fig. S10 and Table S2.† The high-resolution Ru 3p spectrum of the RCO_350 catalyst shown in Fig. 1f is deconvoluted into four sub-peaks, corresponding to the spin orbitals of Ru $3p_{3/2}$ (Ru^{4+} at 462.87 eV, Ru^{3+} at 466.0 eV) and Ru $2p_{1/2}$ (Ru^{4+} at 485.12 eV, Ru^{3+} at 487.75 eV) peaks.[40,41] Compared to the commercial RuO_2, RCO_350 exhibits a shift of approximately 0.87 eV to higher binding energy in the Ru $3p_{3/2}$ XPS peak. Similarly, RCO_400 and RCO_450 present shifts of *ca.* 0.62 eV in the same direction. The Ru $3p_{3/2}$ peak of RCO_*T* shifts to higher binding energy, indicating the elevated oxidation state of Ru. The change is accompanied by an upward shift in the Ru d-band center position. With the increase in temperature, the degree of electron loss in RCO_*T* decreases, correspondingly reducing the magnitude of Ru d-band center upshift.[42]

The high-resolution Co 2p spectrum of the RCO_350 catalyst displayed in Fig. 1g is deconvoluted into seven sub-peaks, corresponding to the spin orbitals of Co $2p_{3/2}$ (Co^{3+} at 779.23 eV, Co^{2+} at 781.29 eV) and Co $2p_{1/2}$ (Co^{3+} at 794.5 eV, Co^{2+} at 796.63 eV) peaks, along with three satellite peaks (784.54 eV, 788.34 eV, and 803.13 eV).[43,44] Compared to Co_3O_4, the Co^{3+} $2p_{3/2}$ XPS of RCO_350, RCO_400, and RCO_450 present the shift of *ca.* 0.49, *ca.* 0.34, and 0.22 eV to the low binding energy. In general, the shifts in Ru 3p and Co 2p XPS spectra indicate an interface interaction between RuO_2 and Co_3O_4 in the RCO_*T* catalysts. As the temperature increases, the magnitude of these shifts decreases, indicating a weakening of the electronic interaction between RuO_2 and Co_3O_4. We hypothesize that the increasing temperature enhances the particles of RuO_2 and Co_3O_4, reducing the interface interaction between them.

Overall, RCO_*T* catalysts synthesized at different temperatures exhibit small particle sizes, contact-rich interfaces, and interaction between RuO_2 and Co_3O_4. As temperature increases, the crystallization degrees of RuO_2 and Co_3O_4 enhance, reducing their interfacial interaction.

The OER performance of RCO_*T* catalysts

The OER performance of the RCO_*T* catalysts was evaluated in 0.10 M $HClO_4$ and compared with commercial RuO_2 and Co_3O_4. The *iR*-compensated LSVs in Fig. 2a demonstrate that the RCO_*T* catalysts exhibit significantly higher activity than the commercial RuO_2 and Co_3O_4. Specifically, the η at 10 mA cm^{-2} for RCO_350, RCO_400, and RCO_450 are 240.6 ± 1.5, 253.3 ± 3.2, and 265.7 ± 4.0 mV, respectively, all of which are lower than those of the commercial RuO_2 and Co_3O_4 (Fig. 2b). Notably, the RCO_350 requires only 275.3 ± 2.1 and 293.7 ± 2.9 mV to reach 30 and 50 mA cm^{-2}, respectively, outperforming RCO_400 and RCO_450. It highlights the superior OER activity of RCO_350 among the RCO_*T* catalysts. The Tafel slopes of the RCO_*T* catalysts, as depicted in Fig. 2c, increase from 59.3 mV dec^{-1} for RCO_350 to 67.2 mV dec^{-1} for RCO_400 and 76.7 mV dec^{-1} for RCO_450. Despite this trend, these values remain significantly lower than the Tafel slope of commercial RuO_2 (171.1 mV dec^{-1}), further confirming the favourable OER kinetics of the RCO_*T* catalysts, particularly RCO_350.

MA is an essential evaluation metric for assessing the performance of catalysts. The MA of the RCO_*T* catalysts was measured at 1.5 V *vs.* RHE. As shown in Fig. 2d, RCO_350 exhibits the highest MA of 137.2 ± 1.2 A g_{Ru}^{-1}, surpassing RCO_400 (96.7 ± 3.1 A g_{Ru}^{-1}) and RCO_450 (68.1 ± 3.6 A g_{Ru}^{-1}). These values are significantly higher than commercial RuO_2, which recorded a much lower MA of 14.6 ± 1.0 A g_{Ru}^{-1}, underscoring the superior activity of the RCO_*T* catalysts. We comprehensively analyzed the C_{dl}, EIS, and SA for the catalysts to gain deeper insights into the factors contributing to the enhanced MA. Fig. 2e shows that the C_{dl} values for the RCO_350, RCO_400, and RCO_450 are 9.1, 4.3, and 3.0 mF cm^{-2}, respectively, significantly higher than that of commercial RuO_2 (0.61 mF cm^{-2}). It indicates that the RCO_*T* catalysts possess a larger ECSA than commercial RuO_2. The observed decreasing trend in C_{dl} from RCO_350 to RCO_450 can be attributed to the particle growth in the elevated

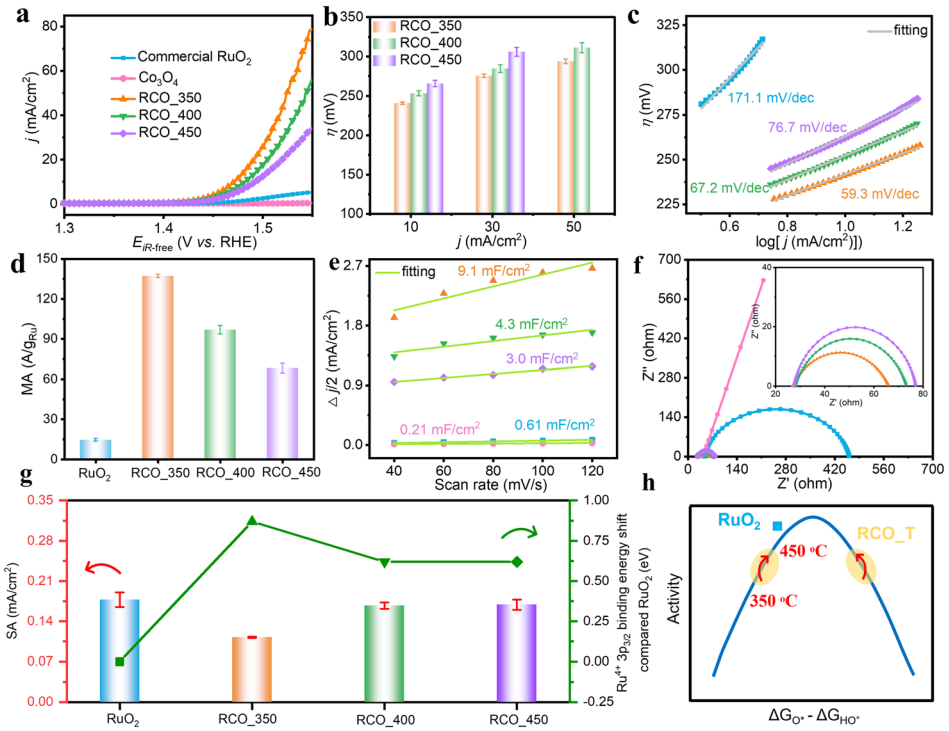

Fig. 2 OER performance of catalysts in 0.1 M $HClO_4$: (a) LSVs, (b) η at different current density, (c) Tafel plot, (d) MA, (e) C_{dl} values, and (f) Nyquist plots at 1.5 V *vs.* RHE. (g) Correlation between the SA and XPS shift of catalysts, (h) the RCO_*T* catalysts activity predicted from volcano plot, where the position of RuO_2 is from ref. 47 and 48.

calcination temperature. The CVs utilized to calculate C_{dl} at various scanning rates are shown in Fig. S11.† Fig. 2f and S12† present the obtained Nyquist plots and equivalent circuits used for curve fitting during EIS analysis. The Nyquist diagrams reveal that the RCO_*T* catalysts exhibit notably lower charge transfer resistance (R_{ct}) than commercial RuO_2 and Co_3O_4, indicating the enhanced charge transfer capability.[45] Among the RCO_*T* catalysts, R_{ct} values increase with calcination temperature, possibly due to reduced interfacial interactions. Overall, enhanced MA in RCO_*T* catalysts originates from their increased ECSA and reduced R_{ct} compared to commercial RuO_2. The superior MA of RCO_350, relative to RCO_400 and RCO_450, can be attributed to its largest ECSA and lowest R_{ct}.

The SA of RCO_*T* catalysts was analyzed, as shown in Fig. 2g, with values of 0.112 ± 0.001 for RCO_350, 0.167 ± 0.005 for RCO_400, and 0.169 ± 0.009 mA cm^{-2} for RCO_450, slightly lower than the commercial RuO_2 (0.178 ± 0.013 mA cm^{-2}). The decreased SA for RCO_*T* catalysts is attributed to their electronic structures, where the Ru^{4+} $3p_{3/2}$ binding energy upshifts demonstrate an inverse relationship with SA. The most pronounced positive shift of 0.87 eV in RCO_350 corresponds to the lowest SA value, while smaller shifts of 0.62 eV in RCO_400/450 result in SA values approaching (but still below) the commercial RuO_2. Based on the volcano plot used for predicting OER activity in Fig. 2h, with the difference between ΔG_{O^*} and ΔG_{HO^*} ($\Delta G_{O^*} - \Delta G_{HO^*}$) as a descriptor, (where O*and HO* are the reaction intermediates adsorbed on the active sites of the catalyst, G_{O^*} and G_{HO^*} are the free energies of the active site with adsorbed O* and HO*),[46–48] and our XPS analysis of the electronic structure of the RCO_*T* catalyst, we propose the following interpretation. The RCO_*T* catalysts exhibit an upward shift of the Ru d-band, enhancing the adsorption of intermediates. For the RCO_400/450 samples, this enhanced adsorption of intermediates induces a symmetrical shift of the $\Delta G_{O^*} - \Delta G_{HO^*}$ values from the left leg to the right leg of the volcano plot. Nevertheless, their OER activity remains comparable to that of the commercial RuO_2. In contrast, the RCO_350 catalyst exhibits a more significant enhancement in intermediate adsorption, causing a pronounced deviation of $\Delta G_{O^*} - \Delta G_{HO^*}$ value from the thermodynamic optimum. This deviation limits its catalytic activity.

We also conducted OER tests of RCO_300. Fig. S13a† shows that the η at 10 mA cm^{-2} of RCO_300 is 307 mV, much higher than that of RCO_*T* catalysts at other temperatures. The CVs utilized to calculate C_{dl} at various scanning rates are shown in Fig. S13b.† Fig. S13c† shows that the C_{dl} value for the RCO_300 is 10.1 mF cm^{-2}. Meanwhile, in Fig. S13d,† its MA is 29.6 A g_{Ru}^{-1}, and its SA is 0.022 mA cm^{-2}. Combined with Fig. 1a, it can be seen that Ru in RCO_300 is in an unoxidized state or amorphous state with a complex structure, and its MA and SA are not better than those of other samples, so we will not give more explanation on it in this work.

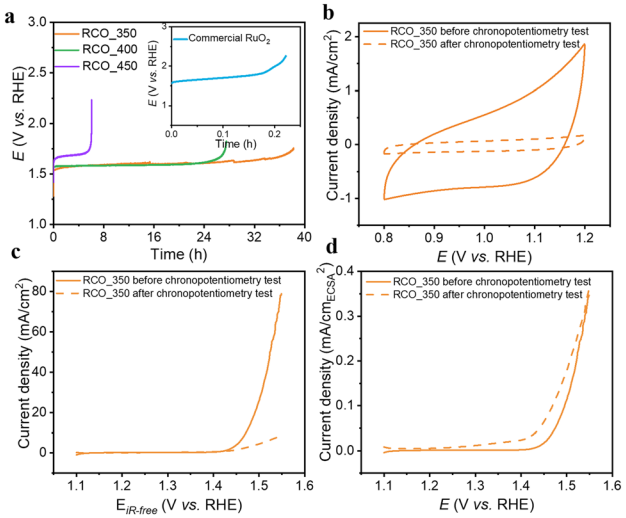

Fig. 3 (a) Electrochemical stability evaluation of the RCO_*T* catalysts and the commercial RuO_2 (the inset) by the chronopotentiometry test at 10 mA cm^{-2}, (b) CV, (c) LSV, (d) SA of RCO_350 before and after chronopotentiometry test.

In addition, stability is an essential indicator in evaluating the catalyst. Chronopotentiometry was conducted to assess the stability of the catalysts. Fig. 3a presents the chronopotentiometry results for RCO_*T* and commercial RuO_2 at 10 mA cm^{-2}. RCO_350, RCO_400, and RCO_450 maintain their performance for 36 h, 26 h, and 5 h, respectively, while the commercial RuO_2 stabilizes for less than 0.2 h. The RCO_*T* catalysts show improved stability than commercial RuO_2, possibly due to the presence of heterogeneous interfaces. Furthermore, as shown in Fig. S14,† RCO_350 outperforms several recently reported noble metal-based electrocatalysts in the acidic solution, surpassing some Ru and Ir-based systems. We further characterized the electrochemical properties and structure changes of RCO_350 after stability testing. As shown in Fig. 3b and S15,† the CV and C_{dl} of RCO_350 are significantly reduced, indicating a significant loss of the active sites in the RCO_350. Fig. S16† shows the SEM image of RCO_350 after the chronopotentiometry test. Although RCO_350 maintains its dodecahedron structure, the particles have grown larger. Tables S3 and S4† show the EDS data, showing that the atomic ratio of Co : Ru shifts from 2.9 : 1 to 9.6 : 1, further confirming the loss of active sites. Fig. 3c and d show that although the apparent activity of RCO_350 decreases significantly after the test, the SA increases compared to before. This indicates that the remaining sites still maintain high activity. The abrupt voltage change observed in RCO_400/450 may be attributed to the continuous loss of active sites in the catalysts during the chronopotentiometry test. Eventually, the remaining active sites are insufficient to sustain 10 mA cm^{-2}, causing the voltage to surge to force the catalyst to continue supplying the required current.

The RCO_*T* catalysts exhibit improved MA and stability compared to commercial RuO_2, as shown in Scheme 2. The enhanced apparent activity can be attributed to the rich, heterogeneous interfaces offering larger ECSA and lower R_{ct}. However, the interfacial interaction between RuO_2 and Co_3O_4 is too strong, leading to over-enhanced adsorption of intermediates, which limits SA further improvement. On the other hand, this strong interaction likely contributes to the enhanced stability of the Ru^{4+}, thereby improving their OER durability.

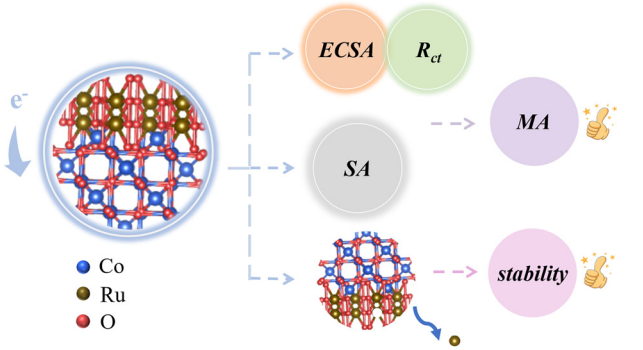

Scheme 2 Schematic illustration of the structure–activity relationship of RCO_*T* catalysts for OER.

PEMWE device performance

In addition to evaluating the performance within the RDE system, it is imperative to investigate the practical implementation of PEMWE. We employed RCO_350 as the anode catalyst for the OER, commercial Pt/C as the cathode catalyst for the HER, and the PEM Nafion® NR115 to assemble a PEMWE cell for testing purposes. Fig. 4a shows the LSVs of RCO_350 and commercial RuO_2 in PEMWE. It is worth noting that when the m_{Ru} of RCO_350 is 0.26 mg cm^{-2}, the voltage to reach 100 mA cm^{-2} is 1.55 V, and when the m_{Ru} of commercial RuO_2 is 0.90 mg cm^{-2}, 1.61 V is required to achieve the same current density. The performance of the RCO_350 catalyst still outperforms the commercial RuO_2. In

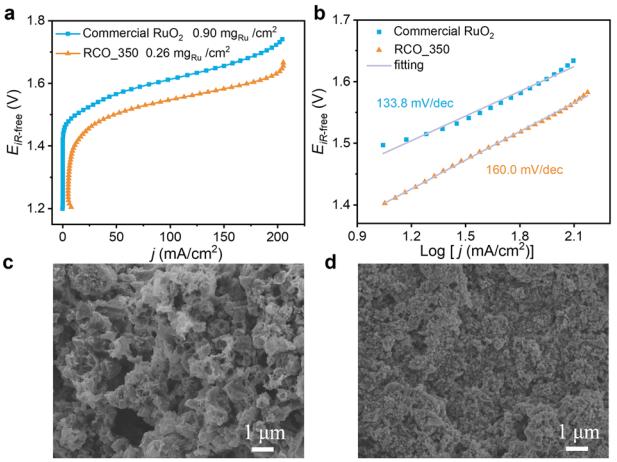

Fig. 4 Electrochemical performances of RCO_350 and commercial RuO_2 on PEMWE devices: (a) LSVs. (b) Tafel plot. SEM images of (c) RCO_350 MEA and (d) commercial RuO_2 MEA.

Fig. 4b, the Tafel slopes for RCO_350 and commercial RuO_2 are 160.0 mV dec^{-1} and 133.8 mV dec^{-1}, respectively. The higher Tafel slope of RCO_350 suggests less favourable OER kinetics, likely due to suboptimal triple-phase boundary conditions within the catalyst layer. As illustrated in Fig. 4c and d, compared to dense commercial RuO_2 MEA, the RCO_350 catalyst layer exhibits a loose and porous structure attributed to the retention of its dodecahedral structures. This morphology may hinder effective contact between the catalyst particles, compromising electrochemical performance.[49,50]

Conclusions

In summary, we developed RCO composite catalysts through temperature-controlled pyrolysis of Ru/ZIF-67 precursors. RCO catalysts synthesized at different temperatures exhibit small particle sizes, contact-rich interfaces, and interaction between RuO_2 and Co_3O_4. As the temperature increases, the particle size of the RCO catalysts grows while the interfacial interaction between RuO_2 and Co_3O_4 weakens. In RDE experiments, the MA and stability of the RCO catalysts are significantly improved. The RCO synthesized at low temperatures exhibits the highest MA due to its smallest particle size, largest ECSA, and lowest R_{ct}. The heterogeneous interfaces between RuO_2 and Co_3O_4 also contributed to the superior stability of the RCO catalysts compared to commercial RuO_2, although ruthenium dissolution remains a limiting factor for long-term performance. In MEA experiments, RCO with low Ru loading demonstrates superior activity to commercial RuO_2. However, the structure of the catalyst layer hinders the construction of the triple-phase boundary. These findings highlight the potential of RCO catalysts for efficient green hydrogen production while underscoring the need for further optimization to address structural challenges in PEMWE applications.

Data availability

The data supporting this article have been included as part of the ESI.†

Author contributions

Yixuan Yuan: writing—original draft, methodology, investigation, visualization. Chang Liu: investigation. Shanshan Liu: investigation. Ruimin Ding: writing—review & editing, supervision, funding acquisition. Xi Yin: conceptualization, methodology, writing, review & editing, supervision, funding acquisition.

Conflicts of interest

There are no conflicts to declare.

Acknowledgements

Financial support from the State Key Laboratory of Coal Conversion, Institute of Coal Chemistry, Chinese Academy of Sciences is greatly appreciated. This study was financially supported by the National Key Research and Development Program of China (2021YFB4001203), the Fundamental Research Program of China Postdoctoral Science Foundation (Grant No. 2022M723263), the State Key Laboratory of Coal Conversion, Institute of Coal Chemistry, Chinese Academy of Sciences (Grant No. SCJC-HN-2023-16, SCJC-HN-2023-17).

Notes and references

1 T. Reier, H. N. Nong, D. Teschner, R. Schlögl and P. Strasser, *Adv. Energy Mater.*, 2017, **7**, 1601275.
2 Z. W. She, J. Kibsgaard, C. F. Dickens, I. Chorkendorff, J. K. Norskov and T. F. Jaramillo, *Science*, 2017, **355**, eaad4998.
3 J. A. Turner, *Science*, 2004, **305**, 972–974.
4 P. K. Katkar, S. J. Marje, S. B. Kale, A. C. Lokhande, C. D. Lokhandea and U. M. Patil, *CrystEngComm*, 2019, **21**, 884–893.
5 C. Spöeri, J. T. H. Kwan, A. Bonakdarpour, D. P. Wilkinson and P. Strasser, *Angew. Chem., Int. Ed.*, 2017, **56**, 5994–6021.
6 F. Y. Chen, Z. Y. Wu, Z. Adler and H. T. Wang, *Joule*, 2021, **5**, 1704–1731.
7 L. A. King, M. A. Hubert, C. Capuano, J. Manco, N. Danilovic, E. Valle, T. R. Hellstern, K. Ayers and T. F. Jaramillo, *Nat. Nanotechnol.*, 2019, **14**, 1071–1074.
8 L. C. Seitz, C. F. Dickens, K. Nishio, Y. Hikita, J. Montoya, A. Doyle, C. Kirk, A. Vojvodic, H. Y. Hwang, J. K. Nørskov and T. F. Jaramillo, *Science*, 2016, **353**, 1011–1014.
9 Y. Lin, Z. Tian, L. Zhang, J. Ma, Z. Jiang, B. J. Deibert, R. Ge and L. Chen, *Nat. Commun.*, 2019, **10**, 162.
10 Y.-R. Zheng, J. Vernieres, Z. Wang, K. Zhang, D. Hochfilzer, K. Krempl, T.-W. Liao, F. Presel, T. Altantzis, J. Fatermans, S. B. Scott, N. M. Secher, C. Moon, P. Liu, S. Bals, S. Van Aert, A. Cao, M. Anand, J. K. Nørskov, J. Kibsgaard and I. Chorkendorf, *Nat. Energy*, 2022, **7**, 55–64.
11 L. Deng, S. F. Hung, Z. Y. Lin, Y. Zhang, C. Zhang, Y. Hao, S. Liu, C. H. Kuo, H. Y. Chen, J. Peng, J. Wang and S. Peng, *Adv. Mater.*, 2023, **35**, 2305939.
12 Z. Y. Wu, F. Y. Chen, B. Li, S. W. Yu, Y. Z. Finfrock, D. M. Meira, Q. Q. Yan, P. Zhu, M. X. Chen, T. W. Song, Z. Yin, H. W. Liang, S. Zhang, G. Wang and H. Wang, *Nat. Mater.*, 2023, **22**, 100–108.
13 Z. S. Li, B. L. Li, M. Yu, C. L. Yu and P. K. Shen, *Int. J. Hydrogen Energy*, 2022, **47**, 26956–26977.
14 C. Wang, L. J. Jin, H. Y. Shang, H. Xu, Y. Shiraishi and Y. Du, *Chin. Chem. Lett.*, 2021, **32**, 2108–2116.
15 X. J. Cao, H. Y. Qin, J. Y. Zhang, X. J. Chen and L. F. Jiao, *J. Am. Chem. Soc.*, 2024, **146**, 32049–32058.
16 Z. H. Yin, H. Liu, J. Hu and J. J. Wang, *Natl. Sci. Rev.*, 2024, **11**, nwae362.

17 T. Y. Gao, D. X. Jiao, L. N. Wang, X. Ge, X. Wen, L. Zhang, L. R. Zheng, X. X. Zou, W. Zhang, W. T. Zheng, J. C. Fan and X. Q. Cui, *J. Am. Chem. Soc.*, 2024, **147**, 4159–4166.
18 N. Zhang and Y. Chai, *Energy Environ. Sci.*, 2021, **14**, 4647–4671.
19 L. An, C. Wei, M. Lu, H. W. Liu, Y. B. Chen, G. G. Scherer, A. C. Fisher, P. X. Xi, Z. C. J. Xu and C. H. Yan, *Adv. Mater.*, 2021, **33**, 2006328.
20 Y. Q. Sun, C. C. Wang, Y. Wang, Y. Xu, X. D. Yang, B. Ouyang and C. C. Li, *Appl. Surf. Sci.*, 2024, **651**, 159222.
21 L. X. Zhou, Y. F. Shao, F. Yin, J. Li, F. Y. Kang and R. T. Lv, *Nat. Commun.*, 2023, **14**, 7644.
22 S. Y. Chen, H. Liu, B. C. Yuan, W. H. Xu, A. Q. Cao, M. G. Sendeku, Y. P. Li, X. M. Sun and F. M. Wang, *Nanoscale*, 2024, **16**, 20940–20947.
23 L. Q. Hou, Z. J. Li, H. Jang, Y. Wang, X. M. Cui, X. M. Gu, M. G. Kim, L. G. Feng, S. G. Liu and X. E. Liu, *Adv. Energy Mater.*, 2023, **13**, 2300177.
24 B. R. KC, D. Kumar and B. P. Bastakoti, *J. Mater. Sci.*, 2024, **59**, 10193–10206.
25 Y. Wu, R. Yao, K. Y. Zhang, Q. Zhao, J. P. Li and G. Liu, *Chem. Eng. J.*, 2024, **479**, 147939.
26 X. Z. Zhang, F. Wu, Q. J. Zhang, Z. Y. Lu, Y. Q. Zheng, Y. A. Zhu and Y. C. Lin, *Inorg. Chem.*, 2024, **63**, 8418–8425.
27 W. Q. Jia, X. J. Cao, X. J. Chen, H. Y. Qin, L. C. Miao, Q. L. Wang and L. F. Jiao, *Small*, 2024, **20**, 2310464.
28 W. Y. Gou, S. S. Zhang, Y. C. Wang, X. H. Tan, L. Q. Liao, Z. N. Qi, M. Xie, Y. Y. Ma, Y. Q. Su and Y. Q. Qu, *Energy Environ. Sci.*, 2024, **17**, 6755–6765.
29 C. L. Rong, S. H. Wang, X. Shen, C. Jia, Q. Sun, Q. Zhang and C. Zhao, *Energy Environ. Sci.*, 2024, **17**, 4196–4204.
30 R. Y. Fan, H. J. Liu, J. K. Ren, Y. C. Li, J. Nan, Y. L. Zhou, C. Y. Liu, Y. M. Chai and B. Dong, *ACS Sustainable Chem. Eng.*, 2024, **12**, 2313–2323.
31 R. Gong, B. W. Liu, X. L. Wang, S. C. Du, Y. Xie, W. Q. Jia, X. X. Bian, Z. M. Chen and Z. Y. Ren, *Small*, 2024, **19**, 2204889.
32 F. F. Shang, H. J. He, Y. Lin, B. An, H. R. Cai, X. Q. Li, W. T. Wang, C. Liang, S. C. Yang and B. Wang, *Inorg. Chem. Front.*, 2024, **11**, 5265–5272.
33 L. L. Liu, M. Zhang, T. T. Ji, J. H. Yan, Y. W. Sun, G. H. He and Y. Liu, *Chem. Mater.*, 2021, **33**, 7350–7356.
34 Y. R. Lin, J. D. Bao, S. T. Zhang, Y. Zhang, J. C. Qiu, Y. F. Li, Y. P. Quan, M. W. Yuan and G. B. Sun, *J. Power Sources*, 2024, **623**, 235394.
35 J. Li, W. Li, G. Liu, Y. Deng, J. Yang and Y. Chen, *Catal. Lett.*, 2016, **146**, 1300–1308.
36 T. Audichon, B. Guenot, S. Baranton, M. Cretin, C. Lamy and C. Coutanceau, *Appl. Catal., B*, 2017, **218**, 385–397.
37 M. Lim, Z. Ma, G. O'Connell, J. A. Yuwono, P. Kumar, R. Jalili, R. Amal, R. Daiyan and E. C. Lovell, *Small*, 2024, **20**, 2401333.
38 F. H. Ye, S. S. Zhang, Q. Q. Cheng, Y. D. Long, D. Liu, R. Paul, Y. M. Fang, Y. Q. Su, L. T. Qu, L. M. Dai and C. G. Hu, *Nat. Commun.*, 2023, **14**, 2040.
39 K. H. Ye, K. S. Li, Y. R. Lu, Z. J. Guo, N. Ni, H. Liu, Y. C. Huang, H. B. Ji and P. S. Wang, *TrAC, Trends Anal. Chem.*, 2019, **116**, 102–108.
40 H. Tang, M. Kong, W. W. Cao, W. G. Ma, J. J. Ding, C. X. Shi, X. D. Yang, Q. S. Shen and Y. Q. Sun, *CrystEngComm*, 2023, **25**, 2473–2478.
41 C. J. Liu, B. B. Sheng, Q. Zhou, D. F. Cao, H. H. Ding, S. M. Chen, P. J. Zhang, Y. J. Xia, X. J. Wu and L. Song, *Nano Res.*, 2022, **15**, 7008–7015.
42 J. Yang, K. An, Z. Yu, L. Qiao, Y. Cao, Y. Zhuang, C. Liu, L. Li, L. Peng and H. Pan, *ACS Catal.*, 2024, **14**, 17739–17747.
43 M. C. Biesinger, B. P. Payne, A. P. Grosvenor, L. W. M. Lau, A. R. Gerson and R. S. C. Smart, *Appl. Surf. Sci.*, 2011, **257**, 2717–2730.
44 Y. M. Zhu, J. A. Wang, T. Koketsu, M. Kroschel, J. M. Chen, S. Y. Hsu, G. Henkelman, Z. W. Hu, P. Strasser and J. W. Ma, *Nat. Commun.*, 2022, **13**, 7754.
45 Y. X. Yao, M. F. Pei, C. Su, X. Jin, Y. P. Qu, Z. H. Song, W. Y. Jiang, X. G. Jian and F. Y. Hu, *Small*, 2024, **20**, 2401481.
46 J. Song, C. Wei, Z. F. Huang, C. Liu, L. Zeng, X. Wang and Z. J. Xu, *Chem. Soc. Rev.*, 2020, **49**, 2196–2214.
47 I. C. Man, H.-Y. Su, F. Calle-Vallejo, H. A. Hansen, J. I. Martínez, N. G. Inoglu, J. Kitchin, T. F. Jaramillo, J. K. Nørskov and J. Rossmeisl, *ChemCatChem*, 2011, **3**, 1159–1165.
48 H. Chen, L. Shi, X. Liang, L. Wang, T. Asefa and X. Zou, *Angew. Chem., Int. Ed.*, 2020, **59**, 19654–19658.
49 J. Kibsgaard and I. Chorkendorff, *Nat. Energy*, 2019, **4**, 430–433.
50 T. T. Phan, S.-K. Kim, J. Islam, M.-J. Kim and J.-H. Lee, *Int. J. Hydrogen Energy*, 2024, **49**, 875–885.
51 C. C. McCrory, S. Jung, J. C. Peters and T. F. Jaramillo, *J. Am. Chem. Soc.*, 2013, **135**, 16977–16987.
52 H. Wu, J. Chang, J. Yu, S. Wang, Z. Hu, G. I. N. Waterhouse, X. Yong, Z. Tang, J. Chang and S. Lu, *Nat. Commun.*, 2024, **15**, 10315.
53 W. X. Zheng, X. X. Cheng, P. P. Chen, L. L. Wang, Y. Duan, G. J. Feng, X. R. Wang, J. J. Li, C. Zhang, Z. Y. Yu and T. B. Lu, *Nat. Commun.*, 2025, **16**, 337.
54 X. Wang, Z. Li, H. Jang, C. Chen, S. Liu, L. Wang, M. G. Kim, J. Cho, Q. Qin and X. Liu, *Adv. Energy Mater.*, 2025, **15**, 2403388.
55 Z. L. Li, H. Y. Sheng, Y. C. Lin, H. Y. Hu, H. F. Sun, Y. Dong, X. W. Chen, L. Z. Wei, Z. Q. Tian, Q. W. Chen, J. W. Su and L. Chen, *Adv. Funct. Mater.*, 2024, **34**, 2409714.